https://doi.org/10.1016/j.apcatb.2023.123048

Modulation of Sulfur Vacancies at $ZnIn_2S_{4-\delta}$/g-C_3N_4 Heterojunction Interface for Successive C-H Secession in Photocatalytic Gaseous Formaldehyde Complete Oxidation

Xinwei Li[1], Yu Huang[2*], Wingkei Ho[3], Shuwen Han[1], Pengge Wang[1,2], Shuncheng Lee[1*], Zhuozhi Zhang[1]

[1] Department of Civil and Environmental Engineering, The Hong Kong Polytechnic University, Hong Kong, China

[2] State Key Laboratory of Loess and Quaternary Geology (SKLLQG) and Key Laboratory of Aerosol Chemistry and Physics, Institute of Earth Environment, Chinese Academy of Sciences, Xi'an 710061, China

[3] Department of Science and Environmental Studies, The Education University of Hong Kong, Hong Kong, China

Corresponding Authors:

Prof. Yu Huang, E-mail: huangyu@ieecas.cn

Prof. Shun-cheng Lee, E-mail: ceslee@polyu.edu.hk

Graphical Abstract

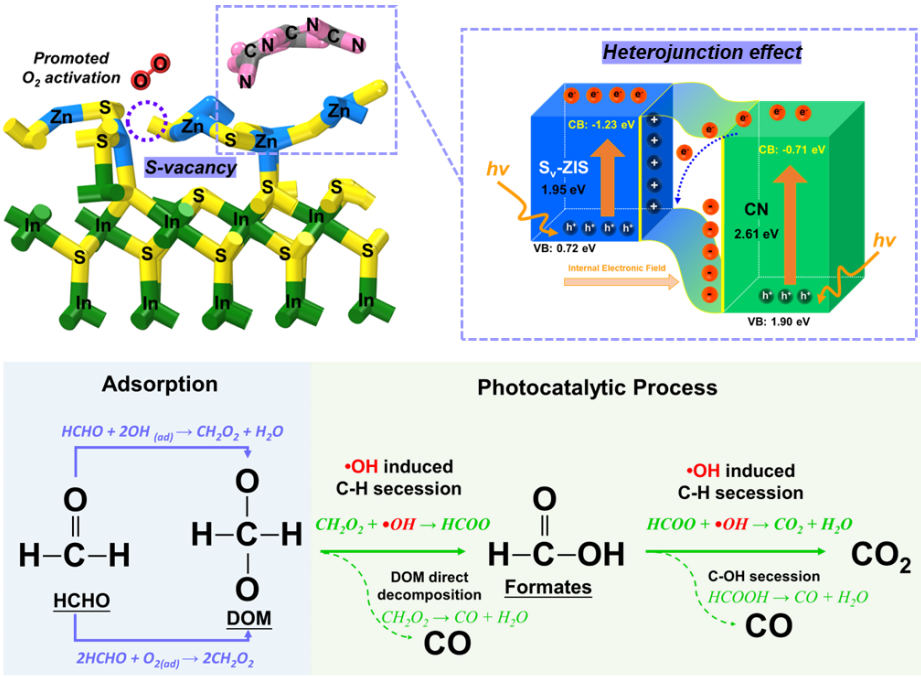

Highlights

- HCHO undergoes complete oxidation via successive •OH-induced C-H bond breakage.
- Heterojunction and vacancy strategies are employed in S_v-$ZnIn_2S_{4-\delta}$/g-C_3N_4 design.
- Heterointerface enhances charge transfer, while S vacancy advances O_2 adsorption.
- Promoted carriers' separation and O_2 activation encourage the $\bullet O_2^- \rightarrow H_2O_2 \rightarrow \bullet OH$ route.

Abstract

Inspired by formaldehyde (HCHO) complete oxidation in atmospheric environments involving hydroxyl radicals (•OH) engaged in the breakage of the carbon-hydrogen (C-H) bond, S_v-$ZnIn_2S_{4-\delta}$/g-C_3N_4 (S_v-ZIS/CN) composite decorated with sulfur vacancies (S-vacancies, S_v) was designed and fabricated for HCHO elimination at ambient environment. $ZnIn_2S_4$ (ZIS) *in-situ* grows on the g-C_3N_4 (CN) flats with an electrostatic attraction effect of cationic precursors, leading to the simultaneous construction of heterojunction interface and generation of S-vacancies. The internal electron field formed at the interface accelerate the photocarriers separation for the surface O_2 activation which has been profited form S-vacancies, thus promoting the generation of •OH radicals from $•O_2^- \rightarrow H_2O_2 \rightarrow$ •OH route. The photocatalytic HCHO oxidation in the S_v-ZIS/5CN sample is kinetically favorable in the presence of abundant •OH engaged in the successive C-H bond scission route dioxymethylene (DOM)→formates(HCOO-)→CO_2 revealed by in-situ DRIFTS, which avoids the generation of undesirable CO and accumulation of intermediates.

Key words: formaldehyde, hydroxyl radicals, photocatalysis, $ZnIn_2S_{4-\delta}$/g-C_3N_4 Heterojunction, C-H secession.

1.1 Introduction

Gaseous formaldehyde (HCHO) is a highly noxious and prevalent volatile organic compound (VOC) in ambient environment. It is classified as a carcinogen by the International Agency for Research on Cancer (IARC) and is known to cause a range of health problems, including eye, nose, and throat irritation; headaches; and allergic reactions.[1-3] In atmospheric environments, the oxidation of HCHO involves hydroxyl radicals (•OH) engaged in the breakage of the carbon-hydrogen (C-H) bond and eventually leading to CO_2 and H_2O at temperatures ranging from 200 to 400 K and pressures up to 760 Torr.[4, 5] The rate constant for the C-H bond breakage increases with growing temperature and pressure, whereas such reactions are energy-intensive and environmentally unfriendly. Given the increasing concerns about public and community health, green methods should be developed to eliminate HCHO in ambient environment.

The photocatalytic degradation of VOCs exploiting reactive oxidate species (ROS) such as •OH oxidation, has garnered significant attention. [6-9] However, the efficiency of photocatalytic reactions is often limited, due to the inadequate transportation of photocarriers and their less affinity with surface O_2.[10] In bulk photocatalyst systems, photogenerated electron-hole recombine easily before reaching to surface reaction sites, and molecular O_2 interacts with coordinatively saturated semiconductor surface mainly through physical adsorption, which can defer the rate of ROS formation.[11] In HCHO photocatalytic process, the inefficient supply of ROS would cause the accumulation of formates (HCOO-) and the incomplete oxidation for the yields of CO instead of CO_2.[12-14] In view of the photocatalytic reactions on the surface of catalysts, nanotechnology modulating strategies should be an effective way to enhance performance. The development of heterojunction provides effective strategies for constructing built-in electric field to achieve efficient charge separation; additionally, vacancy engineering alters the electronic and optical properties of the photocatalyst to facilitate the activation of O_2, leading to the generation of ROS.[15] In this regard, interface design in heterojunction systems and defect engineering is

recognized as two-effective means.[16, 17] However, limited studies have reported on heterostructure-induced vacancy for the application of HCHO complete oxidation.

Herein, we aimed to develop a model catalyst for the application of HCHO degradation by the synergetic effect between heterojunction construction and vacancy creation. Specifically, we designed a S_v-$ZnIn_2S_{4-\delta}$/g-C_3N_4 (S_v-ZIS/CN) composite with sulfur vacancies (S-vacancies, S_v). $ZnIn_2S_4$ (ZIS) is a typical ternary layered metal chalcogenide semiconductor with adjustable band gap of 2.06~2.85eV,[18] and a band gap structure that matches well with g-C_3N_4 (CN), making it possible to construct a binary heterojunction system.[19] The presence of S-vacancies can enhance activity in the selective photocatalytic oxidation of VOCs from previous study.[20-23] In this work, S_v-ZIS/CN composites were facilely fabricated with Zn^{2+} and In^{3+} precursor adsorbed on CN flat in advance, and then followed by a one-step hydrothermal process with thioacetamide (TAA, C_2H_5NS). The content of CN added serves as a variable in the S_v-ZIS/CN composites system, and detailed characterization and simulations were employed to gain in-depth understanding of the physicochemical properties. The as-prepared composites were evaluated for photocatalytic HCHO oxidation in ambient environment. The generation of ROS and the corresponding reaction pathway for HCHO complete degradation will be investigated. A possible mechanism for the photo-catalytic reaction is proposed to guide the design of efficient photocatalyst for VOC degradation.

2. Experimental Section

2.1 Catalyst preparation

All reagents for catalyst synthesis were of analytical grade and used without further purification. g-C_3N_4 (CN) was prepared by 10 g of urea directly calcined at 550 °C for 2 h in air with a heating rate of 15 $^oC \cdot min^{-1}$. The resultant canary powder was collected and denoted as CN.[24] In the representative experiment of the ZIS sample, 1 mmol zinc nitrate hexahydrate [$Zn(NO_3)_2 \cdot 6H_2O$] as Zn^{2+} precursor and 2 mmol indium trinitrate hydrate [$In(NO_3)_3 \cdot 4.5H_2O$] In^{3+} precursor were dissolved in 30 mL of

deionized water, and vigorously stirred at room temperature for 30 min. The solution was added with 5 mmol of thioacetamide (TAA) under ultrasonication and then vigorously stirred for 30 min. The solution was transferred to a 50 mL Teflon-lined stainless-steel autoclave and heated at 160 °C for 2 h. After cooling down to room temperature, ZIS sample was collected by centrifugation, washed several times by using deionized water and ethanol, and dried in an oven at 60 °C for 24 h. The S-vacancies were modulated by constructing heterojunction interfaces simultaneously. Specifically, certain contents of CN were added into Zn^{2+} and In^{3+} precursor solution for 60 min stirring at room temperature to obtain uniform suspension before solvothermal reaction with addition of TAA. The following procedures were the same as ZIS synthesis, and the content of CN added serves as a variable in the S_v-ZIS/CN composite system. The CN contents relied on the mass ratio to the theoretical yield of ZIS. Moreover, 2, 5, 10, and 30 wt.% and as-synthesized samples were donated as S_v-ZIS/2, 5, 10, and 30CN, respectively.

2.2 Photocatalytic activity measurement

photocatalytic HCHO oxidation ability of the as-prepared samples was evaluated in a home-made continuous flow system as our previous work.[25] The volume of the reactor was 0.40 L (20 cm ×10 cm × 2 cm). The distance between the sample surface and the quartz window is about 5.0 mm and the reaction gas can only pass between the surface of the sample and the window. The optical path window is made of quartz glass. Visible light (420 nm cut-off) was vertically provided outside the reactor during the photocatalytic reaction. About 0.10 g of the catalyst was added in distilled water (2.00 mL) and coated onto a glass dish with a diameter of 8.0 cm. The coated dish was pretreated at 60 °C to remove water in the suspension and placed in the center of the reactor after cooling to room temperature. The standard HCHO gas was acquired from a compressed gas cylinder at a concentration of 50.00 ppm of HCHO (N_2 balance). The initial concentration of HCHO was diluted to 1 ppm by the processed air stream with a zero-air initiator (Thermo). The standard air stream and HCHO was mixed in gas

dilution calibrator (Thermo) in advance and the total flow rate was controlled at 1.00 L min^{-1}. After the adsorption-desorption equilibrium was achieved, the lamp was turned on to initiate the reaction. The concentrations of HCHO and HCOO- were measured by an on-line a Photoacoustic IR multi gas monitor (INNOVA Air Tech Instruments Model 1412). The detection limit of HCHO and HCOO- are 0.04 ppm. The entire measurement was conducted under ambient conditions and relative humidity of 30±5%. The HCHO removal ratio (η) and the HCOO- generation rate (*HCOO-%*) were calculated by the following equations. Evaluation test was conducted twice in parallel.

$$\eta\ (\%) = (1- C_t/C_0) \times 100\ \% \quad \text{(Eq. 1)}$$

$$HCOO\text{-}\% = C_{HCOO\text{-}}/C_0 \quad \text{(Eq. 2)}$$

where, C_t is the outlet concentration of HCHO after the reaction, for reaction time *t*; C_0 represents the initial inlet concentration; $C_{HCOO\text{-}}$ refers to the outlet concentration of HCOO- for reaction time *t.*

2.3 Materials characterization

The detailed materials characterization methods are presented in Supporting Information (SI).

2.4 Density function theory (DFT) calculation

Spin-polarized DFT-D2 calculations[26] were carried out utilizing the "Vienna ab initio simulation package" (code VASP 5.4.5),[27, 28] which uses a generalized gradient correlation functional.[29] The detailed calculation set up is described in Supporting Information (SI).

3. Results and discussion

3.1 Modulation of S-vacancies at ZIS/CN heterojunction interface

The as-synthesized samples are characterized by X-ray diffraction (XRD) to identify the crystal phase. The XRD patterns in Fig. 1a of the CN sample matches well with g-

C_3N_4[30], while those of the ZIS sample exhibit distinct peaks consistent with $ZnIn_2S_4$ (JCPDS:65-2023). The S_v-ZIS/CN samples show the same XRD patterns as the ZIS sample, indicating that the main crystal structure is in the phase of $ZnIn_2S_4$. However, the intensity of the diffraction peaks gradually weakened with increasing CN content as CN affects the crystallization of the $ZnIn_2S_4$. Typically, the crystal structure of the S_v-ZIS/30CN sample even tends to be an amorphous state. Fourier-transform infrared spectroscopy (FTIR) was adopted to characterize the surface functional groups. The absorption bands in the 1200−1700 cm^{-1} region and the striking band at 810 cm^{-1} indicate the stretching vibration of the heptazine heterocycles,[31] are observed in both CN and S_v-ZIS/CN samples. Even though the phase structure of CN was not detected in the S_v-ZIS/CN samples from the XRD, the FTIR signals for the heterocycles featured in CN were observed. However, the IR peaks at 890 cm^{-1} together with the broad peak within 3000−3600 cm^{-1} assigned to N-H groups in CN samples were not identified in S_v-ZIS/CN samples.[32] These hydrogen bonds are recognized as the covalent bonding interconnect of polymeric layers in CN, which perceive to induce inefficient intralayer transport of charge carriers from previous studies.[33] The FTIR results indicate the existence of CN functional groups in S_v-ZIS/CN samples with undesired hydrogen bonds destroyed.

Morphology variation is more evident during the development of the S_v-ZIS/CN heterojunction. The scanning electron microscopy (SEM) images show that the pristine ZIS sample has a hierarchical microspheres morphology with a radius of about 2-3 um (Fig. 1c), and are composed of self-assembly of ultrathin nanosheets (Fig. 1d). The morphology of individual CN sample (in Fig. S1) presented to be lamellar nanosheets stacked together, consistent with previous reports.[34] The stacked wrinkled CN sheets wrapped ZIS microsphere were assembled into the S_v-ZIS/CN sample (Fig. 1d, e). The S_v-ZIS/5CN sample with a compound architecture enhanced the specific surface area of 85.76 m^2/g, which is higher than those of the CN sample (67.25 m^2/g) and the ZIS sample (69.33 m^2/g) as measured by Brunauer–Emmett–Teller (BET) method. The nitrogen adsorption–desorption isotherm (Fig.S2a) presents typical type III isotherms, and the Barrett-Joyner-Halenda (BJH) pore size distribution curve (Fig.S2b) indicate

the mesoporous feature of S_v-ZIS/5CN sample at 2−5 nm. The enhanced surface area and pore volume characters increase the utilization of light from nanosheets and cavity to provide more active sites for the following reaction. The corresponding elemental mapping images (Fig. 1i-m) indicate the even dispersion of abundant elements including Zn, In, S, C and N over S_v-ZIS/5CN sample. The transmission electron microscopy (TEM) images clearly present that ZIS microsphere was anchored into CN nanosheet. In the HRTEM image of the Sv-ZIS/5CN sample (Fig. 1h), two different lattice spacing, d1=0.32 nm and d2=0.33 nm, are measured at the interface of CN and ZIS, which are matching with the spacing of the (102) plane of $ZnIn_2S_4$, and the (002) crystal plane of g-C_3N_4[35], respectively. The intimate interface between ZIS and CN is supposed to promote the migration of internal charges.

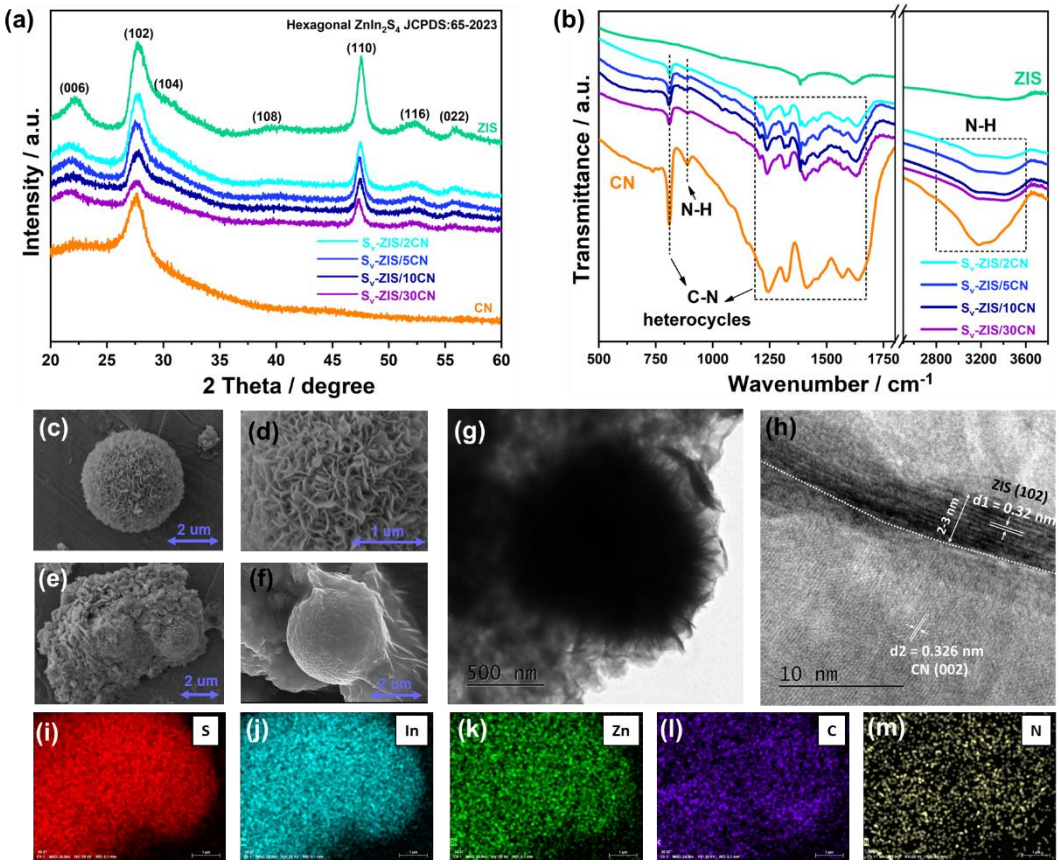

Fig.1. XRD patterns (a) and FITR results (b) of ZIS and S_v-ZIS/CN samples. SEM images of ZIS sample (c, d) and S_v-ZIS/5CN sample (e, f). TEM (g) and HRTEM (h) images of S_v-ZIS/5CN sample. SEM mapping of S_v-ZIS/5CN sample with elements of S (i), In (j), Zn (k), C (l), and N (m) elements.

The chemical composition and states of CN, ZIS and S_v-ZIS/5CN samples are

ascertained by X-ray photoelectron spectroscopy (XPS). In Fig. 2a the XPS survey spectra of Zn, In, S, and C in ZIS and S_v-ZIS/CN samples. The characteristic peaks of N are observed in S_v-ZIS/CN sample. For the N1s spectrum in Fig 2b, three peaks at 398.7, 400.1 and 401.2 eV are ascribed to C-N=C, tertiary N-C_3 groups, and N(CH) groups, respectively.[36] The peak position of N1s exhibits a positive shift compared to CN sample, indicating the charge interaction at the CN and ZIS interface.[37] In the C1s region (Fig 2c), the peak located around 284.8 eV in the samples is assigned to adventitious carbon species.[38] The C1s peak around 288.3 eV in CN and S_v-ZIS/CN samples can be determined to the sp^2-hybridized carbon N-C=N in trizine rings[39, 40]. The binding energy at 293.5 eV is attributed to the C-N-H groups in g-C_3N_4. From the atomic ratio of C/N determined by element analysis in Table S1, the value of CN sample is 3.00/4.20, which is lower than the stoichiometric ratio of C/N with 3.00/4.00 in standard g-C_3N_4 and 1.00/1.22 in the S_v-ZIS/5CN sample. The higher concentration of N in the CN sample commonly originates from residual amine groups, thereby contributing to the formation of hydrogen bonds.[41] The decreased atomic ratio of C/N in the S_v-ZIS/5CN sample also indicate the breakage of hydrogen bonds.

The comparison of the XPS spectra of S2p, Zn2p, and In3d of ZIS and S_v-ZIS/5CN samples are presented in Fig. 2d-f. The atomic ratios of Zn/In/S in the pristine ZIS and S_v-ZIS/CN samples are 1.00/1.95/3.83 and 1.00/1.81/3.14 in Table S1, respectively. The lower S atom ratio in the S_v-ZIS/5CN sample indicates the sulfur loss with the construction of heterojunction. Consequently, the S_v-ZIS/5CN composite exhibits approximately 18% sulfur vacancy content. Besides, based on the S2p XPS spectra in Fig. 2d, the peaks at 163.04 and 162.20 eV of the pristine ZIS sample assigns to S2p1/2 and 2P 3/2, respectively, while the characteristic peaks in the S_v-ZIS/5CN sample have negative shift to 162.85 and 161.84 eV, respectively. This can be attributed to the existence of S-vacancies in the composite that serves as electron-trapping centers to decrease the binding energy of S atoms.[42, 43] The electron paramagnetic resonance (EPR) signal in Fig. S3 located at g=2.002 for S_v-ZIS/5CN sample further verifies the presence of S-vacancies.[44] The binding energies of S_v-ZIS/CN sample at both Zn2p (two deconvoluted peaks $Zn2p_{1/2}$ along with $Zn2p_{3/2}$) in Fig. 2e and In3d (two

deconvoluted peaks $In3d_{3/2}$ together with $In3d_{5/2}$) in Fig. 2f presented a negative shift of about 0.29−0.33 eV and 0.18−0.22 eV compared with that of the ZIS sample. This finding could be due to the low coordination of anion group S^{2-} resulting from the generation of S-vacancies.[45] The binding energy of Zn decreases more evidently than that of In in the S_v-ZIS/5CN sample, indicating the loss of S atoms mostly around Zn atoms.

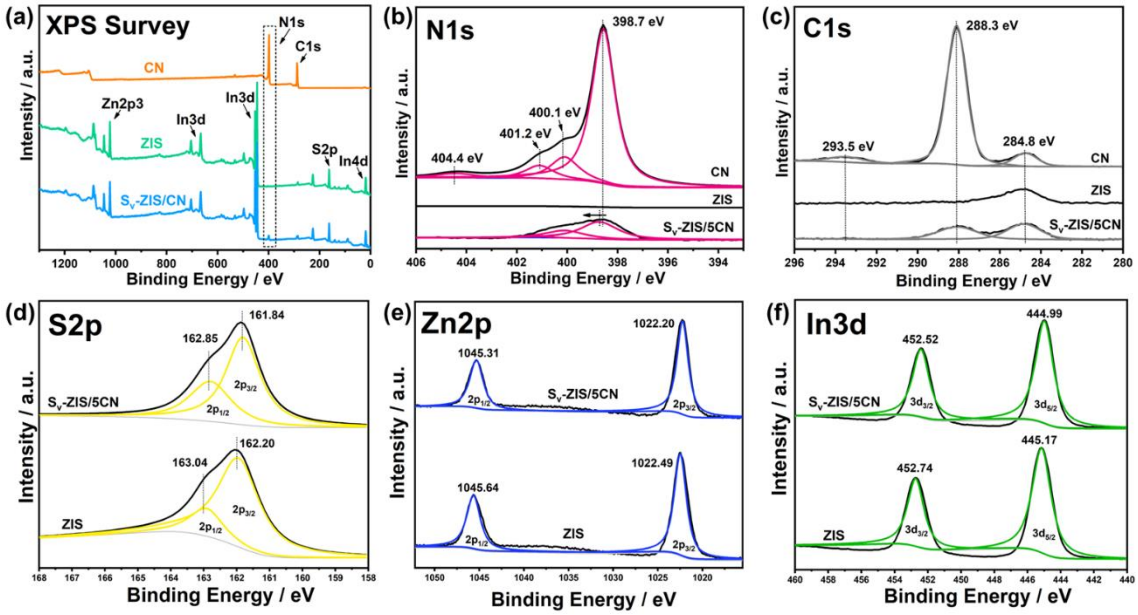

Fig. 2. XPS spectra of survey (a), C1s (b), N1s (c) of CN, ZIS and S_v-ZIS/5CN samples. XPS spectra of S2p (d), Zn2p (e), and In3d (f) of ZIS and S_v-ZIS/5CN sample.

When the CN was dispersed in the aqueous solution containing Zn^{2+} and In^{3+}, the cations were readily loaded on the surfaces of negatively charged CN nanosheet that was verified by zeta potential (Fig. S4) through electrostatic attraction effect.[46] Along with the addition of TAA, the S^{2-} reacted with Zn^{2+} and In^{3+} to grow ZIS on the CNs flat during hydrothermal reaction. Ultimately, ZIS nanospheres are uniformly distributed on the CN flat to obtain S_v-ZIS/CN binary heterojunction system. The overall modulation procedure of S_v-ZIS/CN is presented in Scheme.1. Based on materials characterization, the electron configuration of S_v-ZIS/CN is simulated by density functional theory (DFT) calculation. A group of heptazine heterocyclic ring representing CN was added over the ZIS structure surface, and the S-vacancy was constructed by breaking Zn-S bonds. The optimized electronic configuration of the S_v-

ZIS/CN electronic structure was shown in Fig. S5.

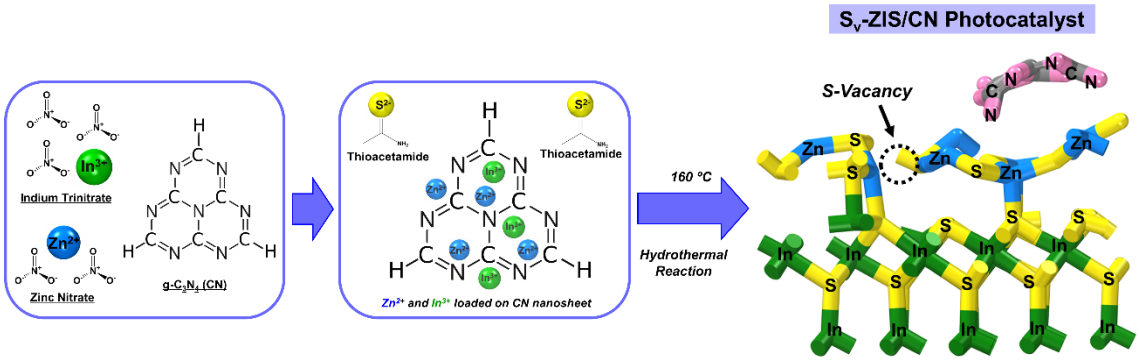

Scheme.1. The formation mechanism of S_v-ZIS/CN composite.

3.2 Photophysical and Electrochemical Properties at the interface

The optical responses of the as-prepared samples are investigated using UV–visible light diffuse reflection spectral system (UV–vis DRS) in Fig 3a. The absorption edge of the S_v-ZIS/CN composites ranges between CN and ZIS sample, and gradually shifts away the visible light area withing increasing CN content. The improved light absorption favors the generation of photocarriers in the presence of visible light. The corresponding band gap energies (E_g) of the CN and ZIS samples are calculated from the plots of the Kubelka-Munk function against the energy of incident light in Fig. 3b with values of 2.61 and 1.95 eV, respectively. [38, 47] According to the Mott–Schottky (M–S plot) in the inset of Fig. 3b, the positive slopes demonstrate the n-type semiconductor traits of CN and ZIS samples. The flat-band potential of CN and ZIS are approximately at the conduction band (CB) potential of semiconductor, which is determined to be -1.23 and -0.71V (vs. NHE) respectively by extending the linear part of electrochemistry M-S plots.[48] Thus the valence band (VB) potentials of CN and ZIS are 1.90 and 0.72V, respectively. From the photoluminescence (PL) spectroscopy (Fig.3c), under 330 nm excitation, the pristine CN displays a prominent emission peak, indicating the intense recombination of photocarriers. Compared with the CN sample, the emission peak intensity of the S_v-ZIS/5CN decreases lightly, which can be contribute to the formation of heterojunction. The photocurrent density in Fig. 3d is in the order of S_v-ZIS/5CN > ZIS > CN under the 420 nm lamp. The highest photocurrent density reveals the most accelerated photocarriers separation and excellent migration

efficiency. In summary, these photo/electrochemical measurements suggest that the construction of Sv-ZIS/5CN sample can accelerate the divorcement efficiency of photogenerated carriers, which are highly favorable for photocatalytic reactions.

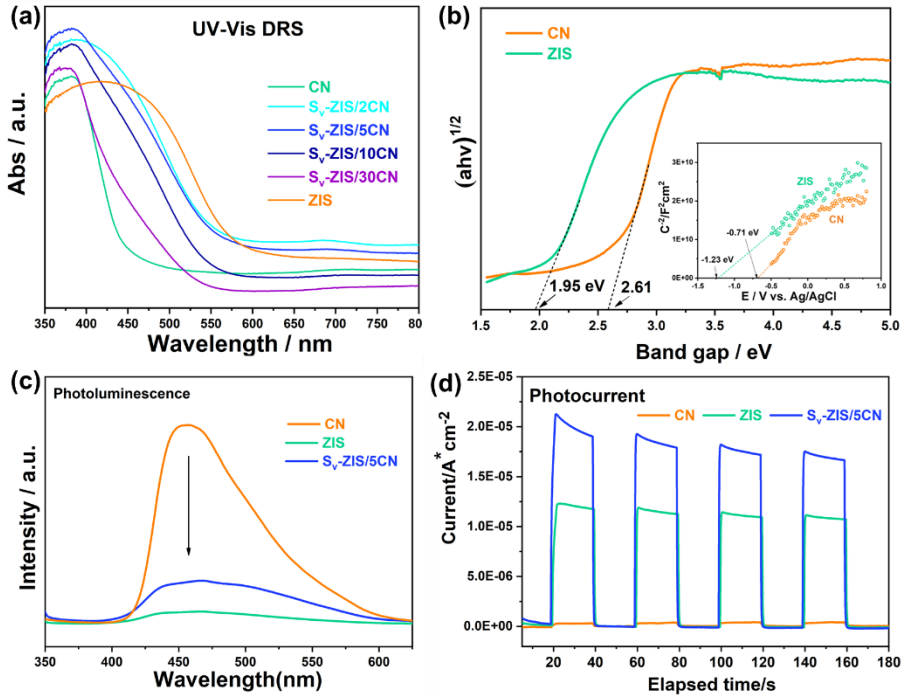

Fig. 3. UV-Vis DRS spectra of as-prepared samples. The Kubelka-Munk function vs. the energy of incident light plots (b) and the M-S plot (b, inset) of ZIS and CN sample. The PL (excited at 330 nm) (c) and photocurrent response (d) of the ZIS, CN, and Sv-ZIS/CN samples under 420 nm irradiation.

DFT calculations were conducted out to reveal the photophysical and electrochemical properties at the interface of S_v-ZIS/CN heterostructure. The surface work functions of S_v-ZIS and CN 4.74 eV (Fig 4a) and 5.29 eV (Fig 4b), respectively. When S_v-ZIS and CN are in close contact, free electrons at S_v-ZIS side with smaller work function spontaneously diffuse to CN with larger work function, creating electron depletion and accumulation near S_v-ZIS and CN, respectively.[49] The uneven charge distribution results in the formation of a built-in electric field from S_v-ZIS side to CN side as depicted in Fig. S6. The charge difference distribution in Fig. 4c of the optimal S_v-ZIS /CN geometry also illustrates the electron cloud density that represents accumulation (blue) and depletion (yellow) on CN and S_v-ZIS, respectively. The total charge (Δq) of CN layer calculated through Bader method is -1.62 e, where the negative value of Δq

represents receiving free electron from the Sv-ZIS side. Accordingly, the photocatalytic charge migration mechanism of S_v-ZIS /CN can be elaborated in Fig. 4d. Under the irradiation of visible light, photoelectrons generated at the CN side will immediately transfer to the S_v-ZIS side with the effect of the coulomb force of the internal electric field, thereby significantly accelerating the photocatalytic carriers transfer, as proven by photocurrent and PL analysis in Fig. 3c and 3d.

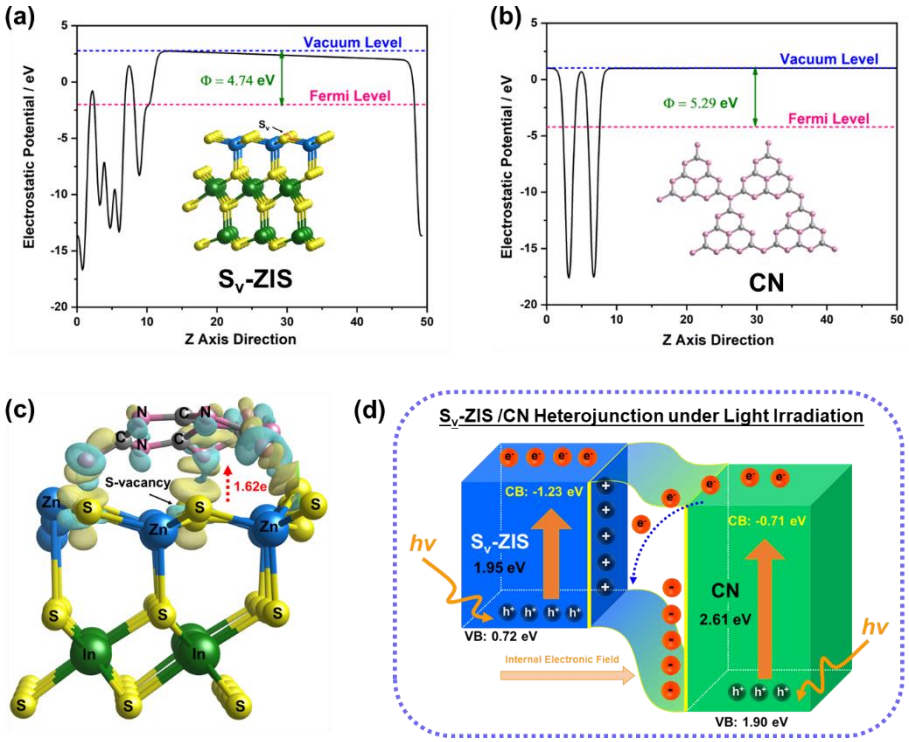

Fig. 4. Work functions of S_v-ZIS surface (a) and CN surface (b); the charge difference distribution of the S_v-ZIS/CN interfacial structure (the charge accumulation region is in blue, and the charge depletion region is in yellow) (c). Schematic diagram of photocatalytic reaction mechanism of S_v-ZIS/CN heterojunction under visible light irradiation.

3.3 O_2 activation and ROS generation

From the band structure deduction, the CB levels of CN and S_v-ZIS possess suitable potential for the reduction of $O_2/\bullet O_2^-$ (-0.33 V vs NHE), while the VB level of neither S_v-ZIS nor CN is lower than the reduction potential for OH/OH^- (+2.3 V vs NHE). Thus, the O_2 activation process from O_2 to $\bullet O_2^-$ via electron transfer is regarded as the first

and the most important step in terms of photocatalytic oxidation. As such, the chemical interaction of O_2 for CN, pristine ZIS and S_v-ZIS/5CN samples were revealed by oxygen temperature-programmed desorption (O_2-TPD) in Fig. 5a. The CN sample appears almost inactive towards O_2 adsorption with negligible TPD signals, while two peaks at approximately 135.1°C and 173.3 °C were observed on the ZIS sample due to physically-adsorbed O_2. [50] Apparently, the S_v-ZIS/5CN sample has enhanced O_2 adsorption capacity to chemisorption with intense TPD signal at 230°C and 334.7°C, implying more chemical adsorption sites for the activation of O_2 with the existence of S-vacancies. [51] The comprehensive insight into the role of S-vacancies was revealed by DFT calculations. The introduction of S-vacancies leads to a significantly enhanced density of states (DOS) at the valence band maximum (VBM) (Fig 5b), which results in electrons being more easily excited to the CB and driving the activation of the surface O_2 than pristine ZIS slab.[21]

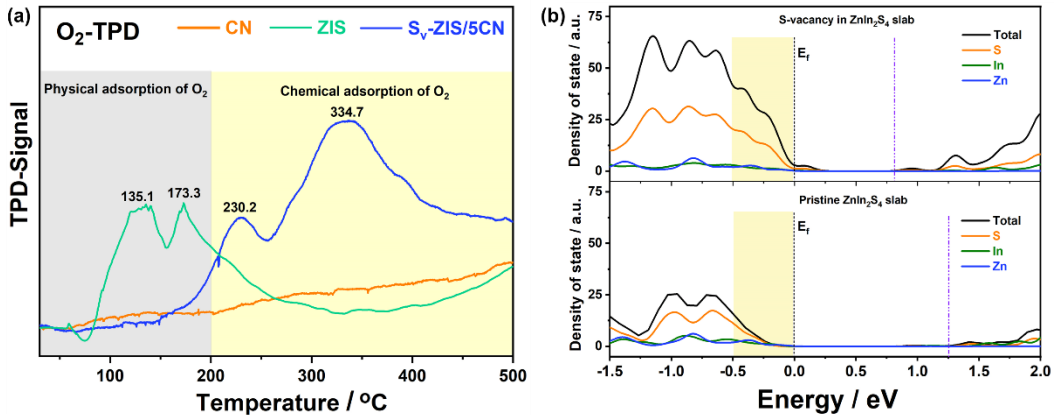

Fig.5. The O_2-TPD of CN, ZIS, and S_v-ZIS/5CN sample (a). Calculated DOS of ZIS and S_v-ZIS slabs (Ef = Fermi level; yellow shading marks the increased DOS around the VBM)

Furthermore, to obtain comprehensive insight into role of heterojunction and vacancies in O_2 activation, the energetically favorable chemisorption process of O_2 on five model structures, namely, CN, ZIS, S_v-ZIS, ZIS/CN, and S_v-ZIS/CN are shown in Fig. S7, and the simulation results were summarized in Table 1. The computed O_2 adsorption energy of saturated CN, ZIS, and ZIS/CN structure are ranged from -0.04 to -0.30 eV. The surface-defected S_v-ZIS/CN and S_v-ZIS configurations show obviously enhanced O_2

adsorption energy to -1.47 eV and -2.16 eV, respectively. The elongation of O-O bond distance enlarged from 1.24 Å in CN and 1.23 Å in ZIS to 1.32 Å in the heterojunction ZIS/CN system, and further enhanced with the introduction of S-vacancies. The O-O bond distance over S_v-ZIS/CN structure was 1.36 Å. The more negative adsorption energy and enhanced O-O bond imply a stronger affinity of O_2 with S-vacancy at the surface. The O_2 activation potential can be ascribed to amount of charge transfer of adsorbed O_2 from the catalysts.[52] Molecule O_2 over ZIS/CN structure received -0.32e electron which is higher than the -0.14e electron over the S_v-ZIS structure, indicating the more promoting effect of charge transfer with heterojunction. With the combined effect of S vacancies and heterojunction, the O_2 over S_v-ZIS/CN structure holds the highest amount of charge transfer with -0.69e. As anticipated, the S_v-ZIS/CN can be employed as an efficient electronic configuration for O_2 activation.

Table 1 Summary of the DFT calculation results of O_2 activation over CN, ZIS, S_v-ZIS, ZIS/CN, and S_v-ZIS/CN model structures

Configuration	E_{ads} / eV	O-O bond length/ Å	O_2 charge / e
CN	-0.11	1.24	-0.06
ZIS	-0.30	1.23	-0.02
S_v-ZIS	-2.16	1.45	-0.14
ZIS/CN	-0.04	1.32	-0.32
S_v-ZIS/CN	-1.47	1.36	-0.69

The activated O_2 affiliated on the surface reacts with photoelectrons to produce $\bullet O_2^-$ ($O_2 + e^- \rightarrow \bullet O_2^-$) (-0.33 V vs NHE) that serve as ROS for photocatalytic oxidation.[20] The direct single-electron routes ($O_2 + 2H^+ + 2e^- \rightarrow H_2O_2$), O_2/H_2O_2 (+0.68 V vs NHE) and continuous two electron ($O_2 + e^- \rightarrow \bullet O_2^- + e^- + 2H^+ \rightarrow H_2O_2$) routes, $H_2O_2/\bullet OH$ (+0.87 V vs NHE) [53] facilitate the generation of H_2O_2 in the system. Although the VB position determined that the photo-generated h^+ cannot oxidize H_2O/OH^- to •OH directly, and that the produced $\bullet O_2^-$ may react with H_2O_2 ($H_2O_2 + \bullet O_2^- \rightarrow \bullet OH + OH^- + O_2$) (+0.31 V vs NHE) for the generation of •OH. [54] The fluorophotometer under visible light was employed to detect H_2O_2 and •OH over ZIS and S_v-ZIS/5CN

samples.[55, 56] In the ZIS sample, H_2O_2 and •OH are measured and gradually increased with irradiation time (Fig. 6a,b). By contrast, a more obvious enhanced quantity of H_2O_2 and •OH was detected in the S_v-ZIS/CN sample (Fig. 6c,d). However, the trends of H_2O_2 and •OH are slightly different as shown in Fig. 6e. The content of •OH in the S_v-ZIS/5CN sample is gradually increasing with reaction, while the content of H_2O_2 initially increases and then decrease indicating the decomposition of H_2O_2.[57] The 5,5-Dimethyl-1-pyrroline N-oxide (DMPO)-trapped ESR measurements were performed to further support the ROS generation. As indicated in Fig. 6f, the characteristic signals of DMPO-•O_2^- are observed after 10 minutes of irradiation with intensity value as follows S_v-ZIS/5CN > ZIS > CN, indicating a large amount of •O_2^- generation in S_v-ZIS/5CN catalyst. The result is in line with O_2 activation ability revealed by DFT calculation. The Fig.6g reveals that the DMPO-•OH signal is not detected for CN due to the weak oxidation potential. However, •OH is detected in the ZIS sample due to the decomposition of H_2O_2. This process is further promoted in the S_v-ZIS/5CN sample with obviously increase in the generation of •OH.

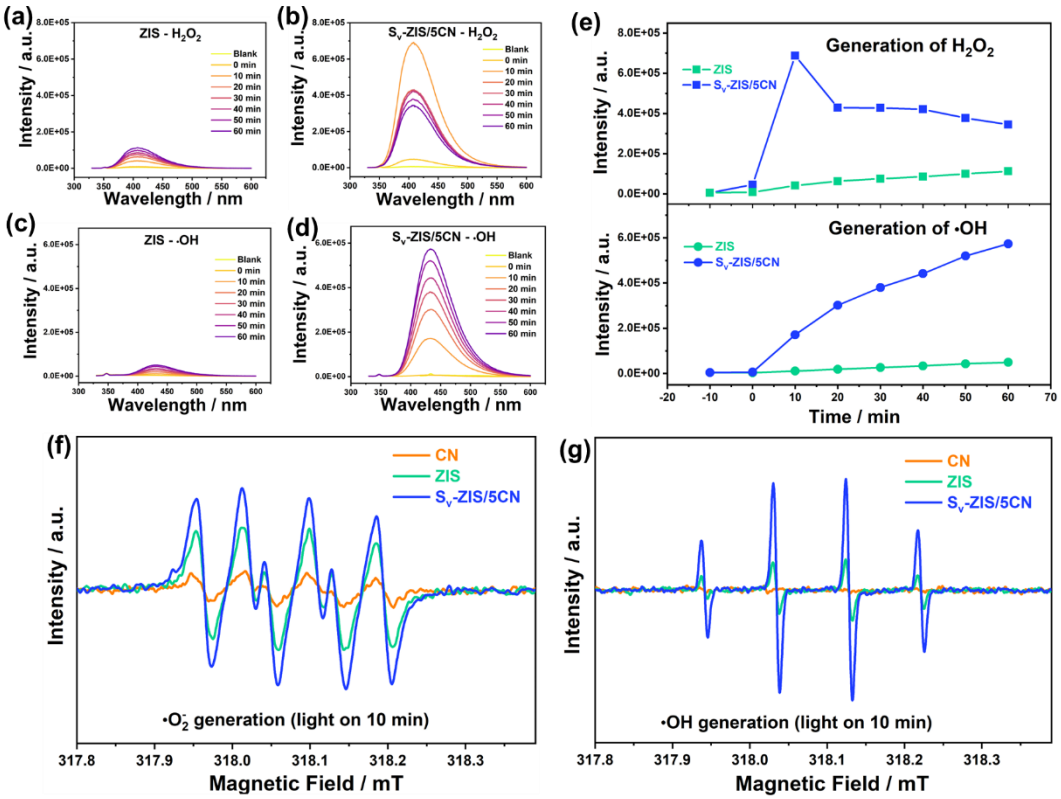

Fig.6. Generation of H_2O_2 in ZIS (a) and S_v-ZIS/5CN (b) samples; generation of •OH

in ZIS (c) and S_v-ZIS/5CN (d) samples by fluorophotometer under visible light. The generation trend of H_2O_2 and •OH in ZIS and S_v-ZIS/5CN samples (e). DMPO-trapped ESR signal under 10-minutes visible light irradiation for the measurement of $•O_2^-$ (f) and •OH (g) of CN, ZIS, and S_v-ZIS/5CN samples.

3.5 Photocatalytic HCHO oxidation activity measurements

Fig.7a shows the photocatalytic degradation rate of HCHO and corresponding HCOO- generation rate with as-prepared samples, and the variations of HCHO concentration inside the reaction chamber presented in Fig. S8. Pristine CN sample exhibits barely photocatalytic activity towards HCHO degradation, and the ZIS sample shows a 19.3% degradation rate towards HCHO. However, 8.3% HCOO- were detected at the same time. Benefiting from the enhanced O_2 activation ability for ROS generation, the HCHO degradation rate of S_v-ZIS/2CN sample and S_v-ZIS/5CN sample are 37.3% and 40.5%, respectively. When the mass ratio of CN part reaches 10.0%, the HCHO degradation activity of the S_v-ZIS/10CN sample decreases to 17.9%, and then to 5.1% in the S_v-ZIS/30CN sample. The lowest formates (HCOO-) generation rate is found in the S_v-ZIS /5CN sample, implying deep oxidation of HCHO. The recycling stability is also an important factor for practical application. As discerned in Fig. 7b, the HCHO degradation rate of the S_v-ZIS /5CN sample remains around 40% with HCOO- generation rate below 1% after 4 cycles of photocatalytic tests.

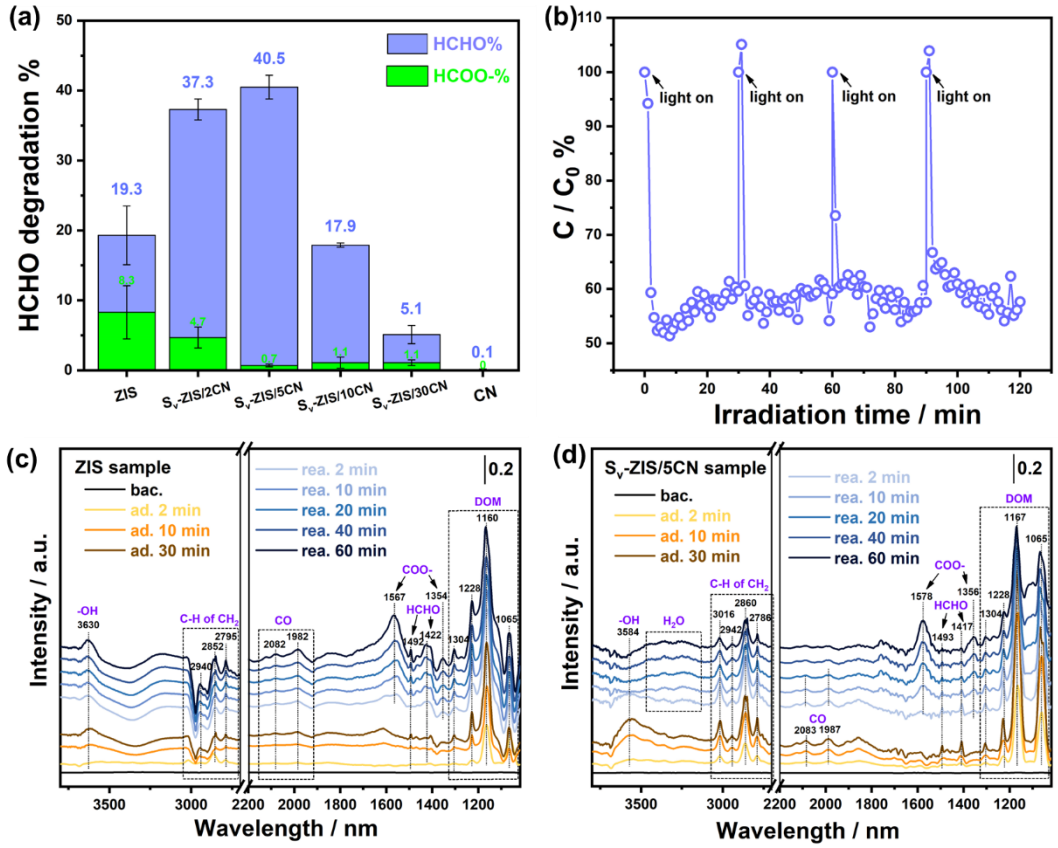

Fig.7 Photocatalytic activities for HCHO degredation and HCOO- genration of as-prepared samples (a) and the repeated photocatalytic test of Sv-ZIS/5CN sample under visible light (b). In situ DRIFTS spectra for the photocatalytic adsorption and reaction of ZIS (c) and Sv-ZIS/5CN sample (d).

To identify the surface species during photocatalytic HCHO degradation, the time dependent *in-situ* diffuse reflectance infrared spectroscopy (*in-situ* DRIFTS) experiments of ZIS and S_v-ZIS/5CN samples from 30-min adsorption process followed by 60-min visible light irradiation were conducted and collected in Fig.7c. In general, in the *in-situ* DRIFTs spectra, the products generated during reaction would display positive peaks.[58] The assignments of IR absorption bands are summarized in Table 2. The intense IR bands of adsorbed dioxymethylene (DOM, -O-CH_2-O-) with different vibration modes at 1065-1304 cm^{-1}, as well as IR peaks centralized from 2786-3016 cm^{-1} were detected in both the ZIS and S_v-ZIS/5CN samples. [59-62] The IR bands at 1417 and 1422 cm^{-1} together with bands 1492 and 1493 cm^{-1} are characteristic of surface adsorbed δ(CHO) and δ(CH_2) of HCHO, respectively. Broad IR peaks at around 3584 and 3630 cm^{-1} are ν(OH) of surface hydroxy (OH). IR peaks at 1354,1356 cm^{-1} and

1576, 1578 cm^{-1} that become discernible over both ZIS and S_v-ZIS/5CN samples after light irradiation are attributed to HCOO- group. Meanwhile, the IR bands of gaseous linearly adsorbed CO species at 1982, 1987, 2083 and 2084 cm^{-1} appear, and the peak intensity gradually grow in ZIS sample.

Table 2 IR peak attributions of *in-situ* DRIFTS spectra

Peak Position / cm^{-1}	Peak Attribution	Ref
1065, 1160, 1167	ν(CO) in DOM	[59]
1228	ν(CH_2) in DOM	[59]
1304	τ(CH_2) in DOM	[60]
1354, 1356	ν_s (OCO) of HCOO- group	[63, 64]
1417, 1422	δ (CHO) of bonded HCHO	[62, 63]
1492,1493	δ (CH_2) of H-bonded HCHO	[62]
1576, 1578	ν_{as} (OCO) of HCOO- group	[63, 64]
1982, 1987, 2083, 2084	Linearly adsorbed CO species	[65, 66]
2786, 2795, 2852, 2860, 2940, 2946, 3016	ν(C-H) and ω(C-H) of CH_2 in DOM	[61, 62]
broad peak at 3400	ν(OH) of surface adsorbed H_2O	[67]
3584, 3630	ν(OH) of surface OH	[68, 69]

More detailed variations of carbonaceous intermediates HCHO, DOM, HCOO-, and CO are represented by the intensity of the featured IR peaks as a function of reaction time (Fig.8). In the adsorption stage, HCHO and DOM are the main species detected in both samples. The DOM is the typical HCHO oxidation intermediates, as the carbonyl group (C=O) of HCHO would reacted with surface O species or OH groups ($HCHO + 2OH \rightarrow CH_2O_2 + H_2O$; $2HCHO + O_2(ad) \rightarrow 2CH_2O_2$) to form DOM even in the dark.[70-72]

Following the photocatalytic reaction, the peak intensities of HCHO and DOM species show slightly increasing trends in the ZIS sample, while clearly decreasing tendency in the S_v-ZIS/5CN sample. Meanwhile, the peak intensities of HCOO- species are increased in both samples when photocatalytic reaction initiated. The difference is that

the rising tendency in the ZIS sample is more intensified than that in the S_v-ZIS/5CN sample. The decline of DOM is expected to be kinetically favorable in the presence of abundant •OH in the S_v-ZIS/5CN sample, which engages in the successive C-H bond scission in the possible reactions, CH_2O_2 + •OH → HCOO and HCOO + •OH → CO_2 + H_2O. However, the insufficient supply of •OH in the ZIS sample may cause HCOO- accumulation on the surface, which is in line with the with photocatalytic activity test results in Fig.7a.

At the same stage, the CO over the ZIS sample appeared in the presence of visible light with the content continuously increases, whereas for the S_v-ZIS/5CN sample, CO only appears at the initial stage and then faded away as the photocatalytic reactions processed. Considering the inadequate •OH of the ZIS sample in the photocatalytic process, DOM may directly recomposite to CO (CH_2O_2 → CO + H_2O), and HCOO- groups prior to C-OH break (HCOOH → CO + H_2O) instead of C-H break. [13] Unfortunately, CO is the non-ideal secondary pollutant during VOC degradation. The IR characterization peaks involving surface hydroxy decrease with peak intensity as the reaction progresses in the S_v-ZIS/5CN sample, which verifies the view that the continuously catalytic reaction consumes the surface hydroxy for the supportive of •OH. However, similar phenomena are not recognized in the ZIS sample. Based on above analysis, the effects of •OH on the C-H bond scission of carbonaceous intermediates in HCHO complete oxidation is presented in Fig.8b.

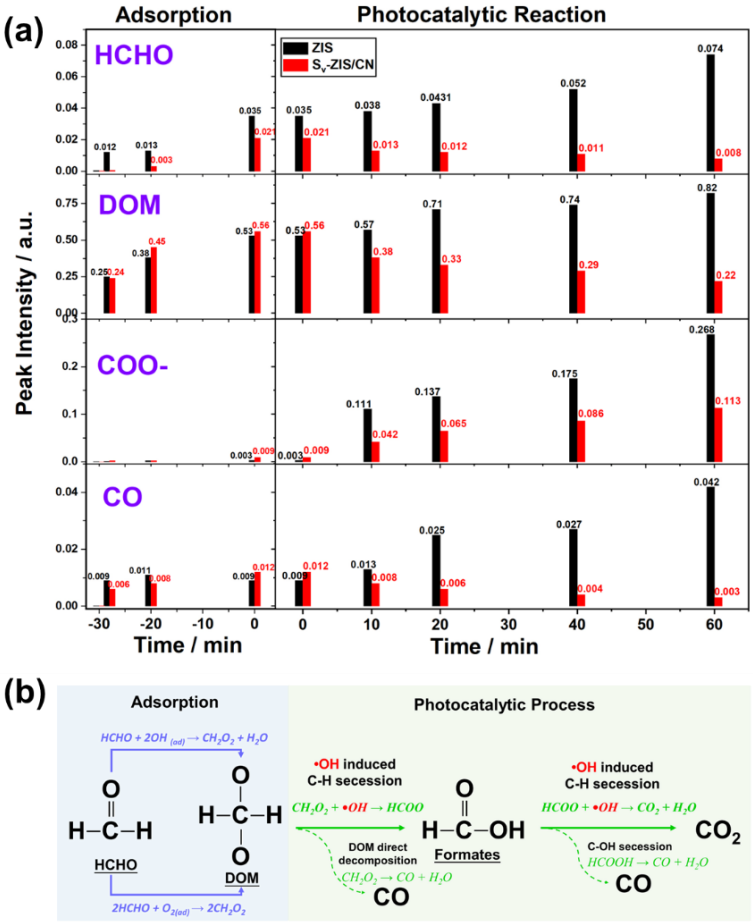

Fig.8 Time dependences of relative intensity of IR bands of ZIS and S_v-ZIS/5CN samples with background subtraction surface of, HCHO (1417 cm^{-1}) DOM (1160 cm^{-1}), HCOO-(1362 cm^{-1}), and CO (2083 cm^{-1}) (a), and HCHO degradation pathway identified by *in-situ* DRIFTS (b).

4. Conclusions

In this work, we successfully modulated S-vacancies at the interface of the S_v-ZIS/CN heterojunction for the photocatalytic oxidation of gaseous HCHO. Owing to the internal electronic fields at the interface of hybrid materials in S_v-ZIS/CN sample, photo-carries transfer and separate efficiently for the surface O_2 activation which has been profited form S-vacancies. This resulted in abundant generation of •OH radicals in the S_v-ZIS/CN sample and excellent performance for the photocatalytic oxidation of HCHO under visible light. The proposed photocatalytic reaction mechanism suggests that the successive C-H bond breakage with sufficient •OH radicals via the route CH_2O_2 →

458 HCOO- → CO_2 is a crucial factor for achieving high selectivity of HCHO complete
459 oxidation products CO_2. This mechanism provides a reasonable explanation for the
460 observed photocatalytic activity and selectivity in the experimental results.
461
462 **CRediT authorship contribution statement**
463 Xinwei Li: Conceptualization, Experiments and DFT simulation, Writing-Original
464 manuscript preparation. Yu Huang: Materials characterization, Resources, Supervision
465 and Organized. Wingkei Ho: Materials characterization, Resources, Writing - Review
466 & Editing. Shuwen Han: Project administration. Pengge Wang: Materials
467 characterization. Shuncheng Lee: Supervision and Methodology. Zhuozhi Zhang:
468 Project administration. All authors discussed the results and commented on the
469 manuscript.
470
471 **Declaration of Competing Interest**
472 The authors declare that they have no known competing financial interests or personal
473 relationships that could have appeared to influence the work reported in this paper.
474
475 **Acknowledgements**
476 This work was supported by the Green Tech Fund (GTF202110151) of Hong Kong
477 SAR Government, Theme-based Research Schemes (T31-603/21-N and T24-504/17-
478 N) of Research Grants Council, Hong Kong. This work was also supported by the
479 General Research Fund (18300920) of Research Grants Council, Hong Kong; Dean's
480 Research Fund (04738), FLASS, EdUHK. This work was also partly supported by the
481 National Key Research and Development Program of China (2016YFA0203000).
482
483

Reference

[1] N. Hanif, N. Hawari, M. Othman, H. Abd Hamid, F. Ahamad, R. Uning, M. Ooi, M. Wahab, M. Sahani, M. Latif, Ambient volatile organic compounds in tropical environments: potential sources, composition and impacts: a review, Chemosphere, 285 (2021) 131355-131367, https://doi.org/10.1016/j.chemosphere.2021.131355.

[2] A. Agency for Toxic Substances and Disease Registry, ToxFAQs™ – for Formaldehyde, https://www.atsdr.cdc.gov/toxfaqs/tfacts111.pdf(2015)

[3] IARC, Formaldehyde, 2-Butoxyethanol and 1-tert-Butoxypropan-2-ol, IARC Monographs on the evaluation of carcinogenic risks to humans, 88 (2006), https://publications.iarc.fr/106

[4] P. Palmer, D. Jacob, A. Fiore, R. Martin, K. Chance, T. Kurosu, Mapping isoprene emissions over North America using formaldehyde column observations from space, J. Geophys. Res. Atmos. 108 (2003)1-9. https://doi.org/10.1029/2002JD002153

[5] J.J. Orlando, G.S. Tyndall, T.J. Wallington, The Atmospheric Chemistry of Alkoxy Radicals, Chem. Rev. 103 (2003) 4657-4690. https://doi.org/10.1021/cr020527p

[6] S. Kuk, S. Ji, S. Kang, D. Yang, H. Kwon, M. Koo, S. Oh, H. Lee, Singlet-oxygen-driven photocatalytic degradation of gaseous formaldehyde and its mechanistic study, Appl. Catal. Environ. B. 328 (2023) 122463-122472. https://doi.org/10.1016/j.apcatb.2023.122463

[7] W. Qu, P. Wang, X. Chen, D. Zhang, Immunizing sulfate-mediated deactivation over TiO_2 photocatalysts for gaseous benzene purification via self-adaptive deoxygenation of sulfate radicals, Appl. Catal. Environ. B. 321 (2023) 122036-122045. https://doi.org/10.1016/j.apcatb.2022.122036

[8] Q. Yu, C. Li, J. Zhao, X. Liu, L. Huang, Y. Zhu, K. Yang, Z. Zhang, D. Ma, Y. Zhang, Efficient photothermal catalytic oxidation of toluene by $La_{1-x}Fe_xMnO_3$ with full spectrum response: the effects of Fe doping and photoactivation, Appl. Catal. Environ. B. 327 (2023) 122441-1224. https://doi.org/10.1016/j.apcatb.2022.122036

[9] X. Zhang, K. Yue, R. Rao, J. Chen, Q. Liu, Y. Yang, F. Bi, Y. Wang, J. Xu, N. Liu, Synthesis of acidic MIL-125 from plastic waste: Significant contribution of N orbital for efficient photocatalytic degradation of chlorobenzene and toluene, Appl. Catal. Environ. B. 310 (2022) 121300-121319, https://doi.org/10.1016/j.apcatb.2022.121300

[10] T. Yoon, M. Ischay, J. Du, Visible light photocatalysis as a greener approach to photochemical synthesis, Nat. Chem. 2 (2010) 527-532. https://doi.org/10.1038/nchem.687

[11] N. Zhang, X. Li, H. Ye, S. Chen, H. Ju, D. Liu, Y. Lin, W. Ye, C. Wang, Q. Xu, Oxide defect engineering enables to couple solar energy into oxygen activation, J. Am. Chem. Soc. 138 (2016) 8928-8935. https://doi.org/10.1021/jacs.6b04629.

[12] J. Li, W. Cui, P. Chen, Y. Chu, J. Sheng, Y. Zhang, Z. Wang, F. Dong, Unraveling the mechanism of binary channel reactions in photocatalytic formaldehyde decomposition for promoted mineralization, Appl. Catal. Environ. B. 260 (2020) 118130-118137, https://doi.org/10.1016/j.apcatb.2019.118130

[13] H. Wang, R. Tang, J. Li, Y. Sun, Z. Wang, K. Kim, F. Dong, Selective breakage of CH bonds in the key oxidation intermediates of gaseous formaldehyde on self-doped $CaSn(OH)_6$ cubes for safe and efficient photocatalysis, Appl. Catal. Environ. B. 277 (2020) 119214-119222, https://doi.org/10.1016/j.apcatb.2020.119214

[14] R. Yang, Q. Chen, Y. Ma, R. Zhu, Y. Fan, J. Huang, H. Niu, Y. Dong, D. Li, Y. Zhang, Highly efficient photocatalytic hydrogen evolution and simultaneous formaldehyde degradation over Z-scheme $ZnIn_2S_4$-NiO/$BiVO_4$ hierarchical heterojunction under visible light irradiation, Chem. Eng.

J. 423 (2021) 130164-130172, https://doi.org/10.1016/j.cej.2021.130164
[15] Y. Huang, Y. Yu, Y. Yu, B. Zhang, Oxygen vacancy engineering in photocatalysis, Sol. RRL, 4 (2020) 2000037, https://doi.org/10.1002/solr.202000037
[16] J. Ma, R. Long, D. Liu, J. Low, Y. Xiong, Defect engineering in photocatalytic methane conversion, Small Structures, 3 (2022) 2100147-2100156, https://doi.org/10.1002/sstr.202100147
[17] Q. Xu, S. Wageh, A. Ghamdi, X.. Li, Technology, Design principle of S-scheme heterojunction photocatalyst, J. Mater. Sci. Technol. 124 (2022) 171-173, https://doi.org/10.1016/j.jmst.2022.02.016
[18] W. Chong, B. Ng, X. Kong, L. Tan, L. Putri, S. Chai, Non-metal doping induced dual pn charge properties in a single $ZnIn_2S_4$ crystal structure provoking charge transfer behaviors and boosting photocatalytic hydrogen generation, Appl. Catal. Environ. B. 325 (2023) 122372 - 122381, https://doi.org/10.1016/j.apcatb.2023.122372
[19] Y. Qin, H. Li, J. Lu, Y. Feng, F. Meng, C. Ma, Y. Yan, M. Meng, Synergy between van der waals heterojunction and vacancy in $ZnIn_2S_4$/g-C_3N_4 2D/2D photocatalysts for enhanced photocatalytic hydrogen evolution, Appl. Catal. Environ. B. 277 (2020) 119254.https://doi.org/10.1016/j.apcatb.2020.119254
[20] Y. Tan, Z. Chai, B. Wang, S. Tian, X. Deng, Z. Bai, L. Chen, S. Shen, J. Guo, M. Cai, C. Au, S. Yin, Boosted Photocatalytic Oxidation of Toluene into Benzaldehyde on $CdIn_2S_4$-CdS: Synergetic Effect of Compact Heterojunction and S-Vacancy, ACS Catal., 11 (2021) 2492-2503. https://doi.org/10.1021/acscatal.0c05703
[21] X. Sun, X. Luo, X. Zhang, J. Xie, S. Jin, H. Wang, X. Zheng, X. Wu, Y. Xie, Enhanced Superoxide Generation on Defective Surfaces for Selective Photooxidation, J. Am. Chem. Soc., 141 (2019) 3797-3801. https://doi.org/10.1021/jacs.8b13051
[22] B. Ng, L. Putri, X. Kong, P. Pasbakhsh, S. Chai, Overall pure water splitting using one-dimensional P-doped twinned $Zn_{0.5}Cd_{0.5}S_{1-x}$ nanorods via synergetic combination of long-range ordered homojunctions and interstitial S vacancies with prolonged carrier lifetime, Appl. Catal. Environ. B. 262 (2020) 118309-118318.https://doi.org/10.1016/j.apcatb.2019.118309
[23] X. Liu, S. Wang, F. Yang, Y. Zhang, L. Yan, K. Li, H. Guo, J. Yan, J. Lin, Construction of Au/g-C_3N_4/$ZnIn_2S_4$ plasma photocatalyst heterojunction composite with 3D hierarchical microarchitecture for visible-light-driven hydrogen production, Int. J. Hydrog. Ener. 47 (2022) 2900-2913, https://doi.org/10.1016/j.ijhydene.2021.10.203
[24] F. Dong, L. Wu, Y. Sun, M. Fu, Z. Wu, S. Lee, Efficient synthesis of polymeric g-C_3N_4 layered materials as novel efficient visible light driven photocatalysts, J. Mater. Chem. A. 21 (2011) 15171-15174, DOI https://doi.org/10.1039/C1JM12844B
[25] X. Li, H. Li, Y. Huang, J. Cao, T. Huang, R. Li, Q. Zhang, S. Lee, W. Ho, Exploring the photocatalytic conversion mechanism of gaseous formaldehyde degradation on TiO_{2-x}-OV surface, J. Hazard. Mater. 424 (2022) 127217-127227, https://doi.org/10.1016/j.jhazmat.2021.127217
[26] S. Grimme, Semiempirical GGA- type density functional constructed with a long- range dispersion correction, J. Comput. Chem., 27 (2006) 1787-1799, https://doi.org/10.1002/jcc.20495
[27] G. Kresse, J. Furthmüller, Efficiency of ab-initio total energy calculations for metals and semiconductors using a plane-wave basis set, Comp. mater. sci., 6 (1996) 15-50, https://doi.org/10.1016/0927-0256(96)00008-0
[28] G. Kresse, J. Furthmüller, Efficient iterative schemes for ab initio total-energy calculations using a plane-wave basis set, Phys. Rev. B, 54 (1996) 11169,

https://doi.org/10.1103/PhysRevB.54.11169
[29] J.P. Perdew, K. Burke, M. Ernzerhof, Generalized gradient approximation made simple, Phys. Rev. Lett., 77 (1996) 3865- 3876 https://doi.org/10.1103/PhysRevLett.77.3865
[30] Z. Li, X. Wang, W. Tian, A. Meng, L. Yang, CoNi Bimetal Cocatalyst Modifying a Hierarchical $ZnIn_2S_4$ Nanosheet-Based Microsphere Noble-Metal-Free Photocatalyst for Efficient Visible-Light-Driven Photocatalytic Hydrogen Production, ACS Sustain. Chem. Eng. 7 (2019) 20190-20201. https://doi.org/10.1021/acssuschemeng.9b06430
[31] Y. Wang, L. Liu, D. Wu, J. Guo, J. Shi, J. Liu, C. Su, Immobilization of metal-organic molecular cage on g-C_3N_4 semiconductor for enhancement of photocatalytic H_2 generation, Chin. J. Catal., 40 (2019) 1198-1204.https://doi.org/10.1016/S1872-2067(19)63387-5
[32] L. Kong, Y. Ji, Z. Dang, J. Yan, P. Li, Y. Li, S. Liu, g-C_3N_4 Loading Black Phosphorus Quantum Dot for Efficient and Stable Photocatalytic H_2 Generation under Visible Light, Adv. Funct. Mater. 28 (2018) 1800668.https://doi.org/10.1002/adfm.201800668
[33] Y. Kang, Y. Yang, L. Yin, X. Kang, L. Wang, G. Liu, H. Cheng, Selective breaking of hydrogen bonds of layered carbon nitride for visible light photocatalysis. Adv. Mater.28 (2016) 6471-6477, https://doi.org/10.1002/adma.201601567
[34] P. Niu, L. Zhang, G. Liu, H. Cheng, Graphene- like carbon nitride nanosheets for improved photocatalytic activities, Adv. Funct. Mater. 22 (2012) 4763-4770. https://doi.org/10.1002/adfm.201200922
[35] F. Dong, Z. Zhao, T. Xiong, Z. Ni, W. Zhang, Y. Sun, W. Ho, In Situ Construction of g-C_3N_4/g-C_3N_4 Metal-Free Heterojunction for Enhanced Visible-Light Photocatalysis, ACS Appl. Mater. Interfaces, 5 (2013) 11392-11401. https://doi.org/10.1021/am403653a.
[36] A. Thomas, A. Fischer, F. Goettmann, M. Antonietti, J. Müller, R. Schlögl, J. Carlsson, Graphitic carbon nitride materials: variation of structure and morphology and their use as metal-free catalysts, J. Mater. Chem. 18 (2008) 4893-4908. https://doi.org/10.1039/B800274F
[37] C. Cheng, S. Zong, J. Shi, F. Xue, Y. Zhang, X. Guan, B. Zheng, J. Deng, L. Guo, Facile preparation of nanosized MoP as cocatalyst coupled with g-C_3N_4 by surface bonding state for enhanced photocatalytic hydrogen production, Appl. Catal. Environ. B. 265 (2020) 118620 - 118630, https://doi.org/10.1016/j.apcatb.2020.118620
[38] Z. Wang, Y. Huang, W. Ho, J. Cao, Z. Shen, S. Lee, Fabrication of $Bi_2O_2CO_3$/g-C_3N_4 heterojunctions for efficiently photocatalytic NO in air removal: In-situ self-sacrificial synthesis, characterizations and mechanistic study, Appl. Catal. Environ. B. 199 (2016) 123-133. https://doi.org/10.1016/j.apcatb.2016.06.027
[39] Q. Lin, L. Li, S. Liang, M. Liu, J. Bi, L. Wu, Efficient synthesis of monolayer carbon nitride 2D nanosheet with tunable concentration and enhanced visible-light photocatalytic activities, Appl. Catal. Environ. B. 163 (2015) 135-142. https://doi.org/10.1016/j.apcatb.2014.07.053
[40] J. Zhang, M. Zhang, G. Zhang, X. Wang, Synthesis of Carbon Nitride Semiconductors in Sulfur Flux for Water Photoredox Catalysis, ACS Catal., 2 (2012) 940-948. https://doi.org/10.1021/cs300167b
[41] B. Lotsch, M. Döblinger, J. Sehnert, L. Seyfarth, J. Senker, O. Oeckler, W. Schnick, Unmasking melon by a complementary approach employing electron diffraction, solid- state NMR spectroscopy, and theoretical calculations—structural characterization of a carbon nitride polymer, Eur. J. Org. Chem., 13 (2007) 4969-4980. https://doi.org/10.1002/chem.200601759
[42] Y. Wang, D. Chen, L. Qin, J. Liang, Y. Huang, Hydrogenated $ZnIn_2S_4$ microspheres: boosting

photocatalytic hydrogen evolution by sulfur vacancy engineering and mechanism insight, Phys. Chem. Chem. Phys. 21 (2019) 25484-25494. https://doi.org/10.1039/C9CP04709C

[43] S. Zhang, X. Liu, C. Liu, S. Luo, L. Wang, T. Cai, Y. Zeng, J. Yuan, W. Dong, Y. Pei, MoS_2 quantum dot growth induced by S vacancies in a $ZnIn_2S_4$ monolayer: atomic-level heterostructure for photocatalytic hydrogen production, ACS Nano, 12 (2018) 751-758. https://doi.org/10.1021/acsnano.7b07974

[44] S. Hu, X. Chen, Q. Li, Y. Zhao, W. Mao, Effect of sulfur vacancies on the nitrogen photofixation performance of ternary metal sulfide photocatalysts, Catal. Sci. & Tech., 6 (2016) 5884-5890. https://doi.org/10.1039/C6CY00622A

[45] J. Bao, X. Zhang, B. Fan, J. Zhang, M. Zhou, W. Yang, X. Hu, H. Wang, B. Pan, Y. Xie, Ultrathin spinel- structured nanosheets rich in oxygen deficiencies for enhanced electrocatalytic water oxidation, Angew. Chem. Int. Ed. 127 (2015) 7507-7512. https://doi.org/10.1002/ange.201502226

[46] W. Chen, T. Liu, T. Huang, X. Liu, X. Yang, Novel mesoporous P-doped graphitic carbon nitride nanosheets coupled with $ZnIn_2S_4$ nanosheets as efficient visible light driven heterostructures with remarkably enhanced photo-reduction activity, Nanoscale, 8 (2016) 3711-3719. https://doi.org/10.1039/C5NR07695A

[47] F. Xu, K. Meng, B. Cheng, S. Wang, J. Xu, J. Yu, Unique S-scheme heterojunctions in self-assembled TiO_2/$CsPbBr_3$ hybrids for CO_2 photoreduction, Nat Commun. 11 (2020) 1-9, https://doi.org/10.1038/s41467-020-18350-7

[48] J. Jing, J. Yang, W. Li, Z. Wu, Y. Zhu, Construction of Interfacial Electric Field via Dual-Porphyrin Heterostructure Boosting Photocatalytic Hydrogen Evolution, Adv. Mater. 34 (2022) 2106807-2106816, https://doi.org/10.1002/adma.202106807

[49] Q. Xu, L. Zhang, B. Cheng, J. Fan, J. Yu, S-scheme heterojunction photocatalyst, Chem. 6 (2020) 1543-1559. https://doi.org/10.1016/j.chempr.2020.06.010

[50] J. Yang, S. Hu, Y. Fang, S. Hoang, L. Li, W. Yang, Z. Liang, J. Wu, J. Hu, W. Xiao, C. Pan, Z. Luo, J. Ding, L. Zhang, Y. Guo, Oxygen Vacancy Promoted O_2 Activation over Perovskite Oxide for Low-Temperature CO Oxidation, ACS Catal., 9 (2019) 9751-9763. https://doi.org/10.1021/acscatal.9b02408

[51] J. He, P. Yao, J. Qiu, H. Zhang, Y. Jiao, J. Wang, Y. Chen, Enhancement effect of oxygen mobility over $Ce_{0.5}Zr_{0.5}O_2$ catalysts doped by multivalent metal oxides for soot combustion, Fuel. 286 (2021) 119359. https://doi.org/10.1016/j.fuel.2020.119359

[52] T. Roongcharoen, S. Impeng, C. Chitpakdee, T. Rungrotmongkol, T. Jitwatanasirikul, S. Jungsuttiwong, S. Namuangruk, Intrinsic property and catalytic performance of single and double metal atoms incorporated g-C_3N_4 for O_2 activation: A DFT insight, Appl. Surf. Sci., 541 (2021) 148671.https://doi.org/10.1016/j.apsusc.2020.148671

[53] L. Wei, S. Liu, H. Wang, Nanostructured $NiCo_2O_4$/$BiVO_4$ heterojunctions for visible-light photocatalytic H_2O-to-H_2O_2 synchronized organic pollutant oxidation, ACS Appl. Nano Mater., 5 (2022) 15378-15388. https://doi.org/10.1021/acsanm.2c03420

[54] B. Bielski, D. Cabelli, R. Arudi, A. Ross, Reactivity of HO_2/O^-_2 Radicals in Aqueous Solution, J Phys. Chem. Ref. Data. 14 (1985) 1041-1100. https://doi.org/10.1063/1.555739

[55] S. Li, G. Dong, R. Hailili, L. Yang, Y. Li, F. Wang, Y. Zeng, C. Wang, Effective photocatalytic H_2O_2 production under visible light irradiation at g-C_3N_4 modulated by carbon vacancies, Appl. Catal. Environ. B., 190 (2016) 26-35.https://doi.org/10.1016/j.apcatb.2016.03.004

[56] G. Dong, L. Yang, F. Wang, L. Zang, C. Wang, Removal of Nitric Oxide through Visible Light Photocatalysis by g-C_3N_4 Modified with Perylene Imides, ACS Catal., 6 (2016) 6511-6519. https://doi.org/10.1021/acscatal.6b01657
[57] J. Geng, L. Zhao, M. Wang, G. Dong, W. Ho, The photocatalytic NO-removal activity of g-C_3N_4 significantly enhanced by the synergistic effect of Pd^0 nanoparticles and N vacancies, Environ. Sci.: Nano, 9 (2022) 742-750. https://doi.org/10.1039/D1EN00937K
[58] K. Li, X. Fang, Z. Fu, Y. Yang, I. Nabi, Y. Feng, A. Bacha, L. Zhang, Boosting photocatalytic chlorophenols remediation with addition of sulfite and mechanism investigation by in-situ DRIFTs, J. Hazard. Mater., 398 (2020) 123007-123017.https://doi.org/10.1016/j.jhazmat.2020.123007
[59] J. Guo, C. Lin, C. Jiang, P. Zhang, Review on noble metal-based catalysts for formaldehyde oxidation at room temperature, Appl. Surf. Sci., 475 (2019) 237-255. https://doi.org/10.1016/j.apsusc.2018.12.238
[60] Z. Yan, Z. Xu, J.G. Yu, M. Jaroniec, Enhanced formaldehyde oxidation on CeO_2/AlOOH-supported Pt catalyst at room temperature, Appl. Catal. B Environ., 199 (2016) 458-465. https://doi.org/10.1016/j.apcatb.2016.06.052
[61] T. Chafik, S. Kameoka, Y. Ukisu, T. Miyadera, In situ diffuse reflectance infrared Fourier transform spectroscopy study of surface species involved in NO_x reduction by ethanol over alumina-supported silver catalyst, J. Mol. Catal. 136 (1998) 203-211.https://doi.org/10.1016/S1381-1169(98)00053-3
[62] Z. Ai, K. Deng, Q. Wan, L. Zhang, S. Lee, Facile Microwave-Assisted Synthesis and Magnetic and Gas Sensing Properties of Fe_3O Nanoroses, J. Phys. Chem. C, 114 (2010) 6237-6242. https://doi.org/10.1021/jp910514f
[63] F. Rotzinger, J. Kesselman-Truttmann, S. Hug, V. Shklover, M. Grätzel, Structure and vibrational spectrum of formate and acetate adsorbed from aqueous solution onto the TiO_2 rutile (110) surface, J. Phys. Chem. B. 108 (2004) 5004-5017, https://doi.org/10.1021/jp0360974
[64] C. Mendive, T. Bredow, M. Blesa, D. Bahnemann, ATR-FTIR measurements and quantum chemical calculations concerning the adsorption and photoreaction of oxalic acid on TiO_2, Phys. Chem. Chem. Phys. 8 (2006) 3232-3247. https://doi.org/10.1039/B518007B
[65] J. Lin, B. Qiao, L. Li, H. Guan, C. Ruan, A. Wang, W. Zhang, X. Wang, T. Zhang, Remarkable effects of hydroxyl species on low-temperature CO (preferential) oxidation over Ir/$Fe(OH)_x$ catalyst, J. Catal., 319 (2014) 142-149.https://doi.org/10.1016/j.jcat.2014.08.011
[66] J. Lin, L. Li, X. Pan, X. Wang, Y. Cong, T. Zhang, S. Zhu, Catalytic decomposition of propellant N_2O Over Ir/Al_2O_3 catalyst, AIChE. J. 62 (2016) 3973-3981.https://doi.org/10.1002/aic.15324
[67] Y. He, H. Ji, In-Situ DRIFTS Study on Catalytic Oxidation of Formaldehyde over Pt/TiO_2 under Mild Conditions, Chin. J. Catal., 31 (2010) 171-175.10.3724/sp.j.1088.2010.90904
[68] Z.X. Yan, Z.H. Xu, J.G. Yu, M. Jaroniec, Effect of microstructure and surface hydroxyls on the catalytic activity of Au/AlOOH for formaldehyde removal at room temperature, J. Colloid Inter. Sci., 501 (2017) 164-174. https://doi.org/10.1016/j.jcis.2017.04.050
[69] S. Sun, J. Ding, J. Bao, C. Gao, Z. Qi, C. Li, Photocatalytic Oxidation of Gaseous Formaldehyde on TiO_2: An In Situ DRIFTS Study, Catal. Lett., 137 (2010) 239-246. https://doi.org/10.1007/s10562-010-0358-4
[70] Q. Yuan, Z. Wu, Y. Jin, F. Xiong, W. Huang, Surface Chemistry of Formaldehyde on Rutile TiO_2(110) Surface: Photocatalysis vs Thermal-Catalysis, J. Phys. Chem. Lett., 118 (2014) 20420-20428. https://doi.org/10.1021/jp5061733

[71] G. Busca, J. Lamotte, J. Lavalley, V. Lorenzelli, FT-IR study of the adsorption and transformation of formaldehyde on oxide surfaces, J. Am. Chem. Soc. 109 (1987) 5197-5202, https://doi.org/10.1021/ja00251a025

[72] T. Kecskés, J. Raskó, J. Kiss, FTIR and mass spectrometric studies on the interaction of formaldehyde with TiO_2 supported Pt and Au catalysts, Appl. Catal. A: Gen. 273 (2004) 55-62, https://doi.org/10.1016/j.apcata.2004.06.012